# Transition and Turbulence Modeling for the Prediction of Cavitating Tip Vortices

Liebrand, Rens; Klapwijk, Maarten; Lloyd, Thomas; Vaz, Guilherme

**DOI**
10.1115/1.4048133

**Publication date**
2021

**Document Version**
Final published version

**Published in**
Journal of Fluids Engineering, Transactions of the ASME

**Rens Liebrand**
Maritime Research Institute Netherlands (MARIN),
Haagsteeg 2,
Wageningen 6708 PM, The Netherlands;
Faculty of Aerospace Engineering,
Delft University of Technology,
Mekelweg 5,
Delft 2628 CD, The Netherlands
e-mail: rensliebrand@gmail.com

**Maarten Klapwijk**[1]
Faculty of Mechanical, Maritime and Material Engineering,
Delft University of Technology,
Mekelweg 2,
Delft 2628 CN, The Netherlands;
MARIN,
Wageningen 6708 PM, The Netherlands
e-mail: m.d.klapwijk@tudelft.nl

**Thomas Lloyd**
MARIN,
Wageningen 6708 PM, The Netherlands
e-mail: t.lloyd@marin.nl

**Guilherme Vaz**
WavEC Offshore Renewables,
Edifício Diogo Cão,
Doca de Alcântara Norte,
Lisbon 1350-352, Portugal;
MARIN,
Wageningen 6708 PM, The Netherlands
e-mail: guilherme.vaz@wavec.org

# Transition and Turbulence Modeling for the Prediction of Cavitating Tip Vortices

*This study evaluates the influence of transition and turbulence modeling on the prediction of wetted and cavitating tip vortices for an elliptical wing, while investigating the numerical errors. Transition modeling increases the quality of numerical predictions since the assumption of a fully turbulent boundary layer, commonly found in literature, contributes to underprediction of the tip vortex cavity size. By applying the local correlation-based transition model (LCTM) and controlling the boundary layer thickness using different turbulent inflow conditions, the pressure in the vortex was found to reduce by 20% for an Angle of Attack (AoA) of 5 deg. The consequent increase in cavity size was found to be of a similar order of magnitude. At 9 deg AoA, transition always occurs just downstream of the leading edge, making this AoA more suitable to investigate the effect of different turbulence modeling approaches. Azimuthal and axial velocity fields are validated against stereographic-particle image velocimetry (S-PIV) measurements. The time-averaged velocity profiles predicted by delayed detached-eddy simulation (DDES) and improved delayed detached-eddy simulation (IDDES) are close to the experiments; however, no velocity fluctuations and vortex dynamics are observed around the vortex. A comparison of wetted and cavitating simulations shows that the cavity leads to a change in the balance between production and destruction of turbulence kinetic energy, which reduces the turbulent diffusion in and around the cavity compared to wetted flow conditions. Consequently, the vapor flow exhibits the characteristics of a potential flow. Whether this is physically plausible remains to be investigated.* [DOI: 10.1115/1.4048133]



## 1 Introduction

There is increased awareness of the harmful environmental impact of underwater radiated noise generated by marine traffic [1,2], as well as increasing attention for on-board comfort [3,4]. Cavitating propeller tip vortices are known to be one of the main contributors to ship noise, due to their dynamic behavior and distinct broadband sound spectrum [5]. To minimize underwater radiated noise, it is therefore desirable to predict the occurrence of tip vortex cavitation and their noise generation during the design process [6,7].

Although flow-field measurements of cavitating vortices have previously been made [8–10], such experiments are not suitable for design purposes, with computational fluid dynamics (CFD) offering the potential to gain additional insight into the details of the flow at reasonable cost. However, knowledge regarding the prediction of the dynamics of tip vortex cavitation is still insufficient to obtain reliable numerical results in relation to noise predictions [11–13]. Therefore, further research into CFD predictions of cavitating flows is required, using simplified test cases. In this study, an elliptical planform with a NACA $66_2$-415 cross section (known as the "Arndt" [14] wing) with a root chord-based Reynolds number $Re = 8.95 \times 10^5$ is used, since stereographic-particle image velocimetry (S-PIV) measurements of the vortex (in wetted and cavitating flow conditions) are available in open literature [10]. Numerical results in the literature often exhibit a premature decay of vorticity, and therefore an underpredicted cavity size, compared to experiments. This is primarily attributed to numerical diffusion, and overprediction of eddy viscosity. Results in literature apply a range of different turbulence models, resulting in a range of different reported lift coefficients, as shown in Fig. 1. Formulations relying on the Boussinesq hypothesis are not sufficient, as shown by Ref. [11]. Curvature corrections are found to improve results but modeling errors of the velocity profiles in the vortex were still found to be large [11,16]. The application of large eddy simulation (LES) and implicit large eddy simulation decreases the modeling error for the integral quantities compared to experiments and the models avoided early decay of vorticity [12]. However, it is unclear whether turbulent velocity fluctuations are properly developed, meaning that the predicted vortex could be excessively laminar. Paskin [13] obtained velocity fluctuations in the wake of the wing using detached eddy simulation (DES). However, due to grid induced separation, the lift coefficient did not match the experimental results of Ref. [10]. Finally, Pereira et al. [17] employed a Reynolds stress model (RSM) to simulate the tip vortex of a rectangular planform with a NACA 0012 profile at 10 deg AoA. It was shown that the model was able to accurately predict the pressure in the center of the wetted flow vortex within the extent of available validation data.

[1]Corresponding author.

Contributed by the Fluids Engineering Division of ASME for publication in the Journal of Fluids Engineering. Manuscript received January 27, 2020; final manuscript received July 20, 2020; published online October 5, 2020. Assoc. Editor: Ning Zhang.

  

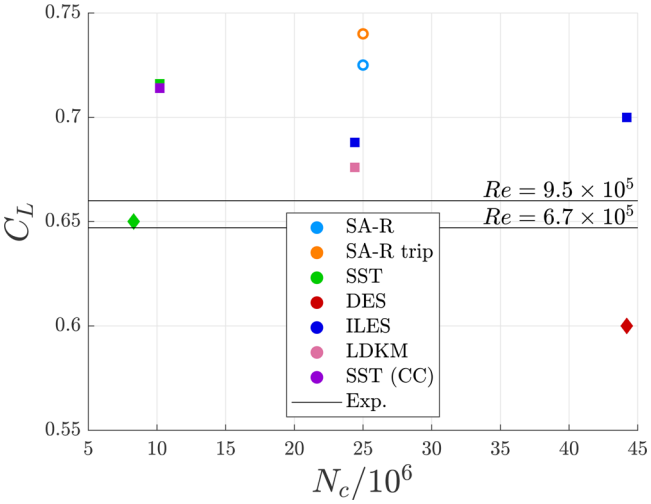


**Fig. 1 Reported lift coefficients ($C_L = L/(1/2\rho U_\infty^2 A)$) versus number of grid cells ($N_c$) for the Arndt wing at 9 deg AoA at two different Reynolds numbers in the computations, $Re = U_\infty c_0/\nu = 6.8\times10^5$ (nonfilled symbols) and $Re = 8.95\times10^5$ (filled symbols). Colors indicate employed turbulence models. Numerical results by Refs. [11] (circles), [13] (diamonds), and [12] (squares). Experimental results obtained by Ref. [15] (horizontal lines).**

It is noteworthy that all approaches in literature assume a fully turbulent boundary layer for the present test case, while the Reynolds number ($8.95 \times 10^5$) lies in the transitional regime, and decreases along the wing toward the tip. This study investigates the hypothesis that this assumption contributes to the underpredicted cavity sizes reported in literature. This hypothesis is considered both theoretically and numerically, using the local correlation-based transition model (LCTM), for both wetted and cavitating flow conditions. To investigate the effect of turbulence models on the vortex, different approaches are employed. A number of Reynolds-averaged Navier–Stokes (RANS) approaches are tested. The popular $k-\omega$ shear stress transport (SST) model [18], and the $k-\sqrt{k}L$ (KSKL) model [19] are both two-equation models, which make use of the Boussinesq hypothesis. The KSKL model is expected to predict lower eddy viscosity than the SST, which may affect the flow inside the vortex. Since anisotropy of the Reynolds stresses may be important, an explicit algebraic Reynolds stress model (EARSM) [20] and RSM [21] are also investigated. Finally, two scale resolving simulation models are applied, which make a different distinction between modeled and resolved turbulence regions: delayed detached-eddy simulation (DDES) [22] and improved delayed detached-eddy simulation (IDDES) [23].

The paper is structured as follows: Section 2 derives the theoretical relation which forms the basis for the hypothesis concerning the effect of including transition on the cavity size. The mathematical transition and turbulence models are given in Sec. 3. Section 4 presents the verification and validation strategy, and Sec. 5 the numerical setup. Results concerning transition and turbulence modeling are presented in Secs. 6 and 7, respectively. Finally, Sec. 8 describes the conclusions.

## 2 Theoretical Argumentation for Applying Transition Modeling

The hypothesis that the fully turbulent boundary layer assumption affects the results is suggested by the reported observations from the original experiments for this test case by Ref. [24]. It was observed that "the tip vortex of the wing mainly interacts with the boundary layer on the suction side, boundary layer fluid is entrained in the vortex which affects the core radius." When we combine this observation with the McCormick hypothesis [25], which relates the boundary layer thickness to the state of the boundary layer, we obtain the relationship

$$\eta_v \propto \delta_s \propto \mathrm{Re}_c^{-h} \tag{1}$$

Here, $\eta_v$ denotes the viscous core radius of the tip vortex, $\delta_s$ the boundary layer thickness on the suction side of the wing, and $\mathrm{Re}_c = U_\infty c/\nu$ the chord-based Reynolds number, with $U_\infty$ the freestream velocity, $c$ the local chord length, and $\nu$ the kinematic viscosity. The constant $h$ accounts for the state of the boundary layer; for a flat plate, this is typically around 0.2 for a fully turbulent boundary layer and 0.4 for a transitional boundary layer [25].

The pressure in the vortex can be linked to the state of the boundary layer, by combining Eq. (1) with two-dimensional semi-analytical expressions for the velocity and pressure distributions in a noncavitating vortex

$$p(\eta = 0) - p_\infty = p_{\min} - p_\infty = -\frac{\rho\Gamma_\infty^2}{(2\pi\eta_v)^2}\zeta\ln(2) \tag{2}$$

Bosschers [6] derived this expression by supplementing the Lamb–Oseen vortex [26] with jump relations for the mass transfer and shear stress as boundary conditions at the vapor–liquid interface. In Eq. (2), $p_\infty$ is the freestream pressure, $\zeta = 1.2564$, a constant to ensure that the azimuthal velocity is maximum at the viscous core radius, and $\Gamma_\infty$ the freestream circulation of the vortex. The latter is related to the circulation over the wing ($\Gamma_0$) through the roll-up process. Analytical expressions to relate the freestream circulation to $\Gamma_0$ exist (e.g., by Refs. [27] and [28]). However, [11] observed that the roll-up process is finished between $1.0 < x/c_0 < 2.0$, resulting in the assumption that $\Gamma_\infty \approx \Gamma_0$ in this work. Combining Eqs. (1) and (2) yields the following proportionality

$$p(\eta = 0) \propto (\Gamma_0/\eta_v)^2 \propto (\Gamma_0/\delta_s)^2 \propto (\Gamma_0/\mathrm{Re}_c^{-h})^2 \tag{3}$$

which shows that the pressure in the core of the vortex is related to the state of the boundary layer on the suction side of the wing and the wing's circulation.

In CFD, the state of the boundary layer can be modified by applying a transition model. Compared to the fully turbulent boundary layer in traditional RANS turbulence models, the use of a transition model yields a laminar boundary layer, which may then transition to a turbulent boundary layer. This leads to a thinner boundary layer which, according to the theory above, should yield a smaller viscous core radius. The resulting larger pressure difference between the freestream and the core pressure of the vortex should therefore lead to a larger cavity. Section 6 investigates to what extent the assumption of a fully turbulent boundary layer in CFD simulations contributes to the underprediction of the cavity sizes as published in prior research [11–13].

## 3 Mathematical Models

In this work, different approaches for solving the Navier–Stokes equations are employed. All approaches decompose the instantaneous quantities, $\Phi$, into a resolved, $\langle\Phi\rangle$, and a modeled (unresolved) component, $\phi$. Applying this decomposition to the unsteady mass conservation and Navier–Stokes equations for a Newtonian fluid including phase change by cavitation yields

$$\frac{\partial\rho}{\partial t} + \frac{\partial\langle\rho U_i\rangle}{\partial x_i} = \left(\frac{1}{\rho_v} - \frac{1}{\rho_l}\right)\dot{m} \tag{4}$$

and

$$\frac{\mathrm{D}\langle\rho U_i\rangle}{\mathrm{D}t} = -\frac{\partial\langle P\rangle}{\partial x_i} + \nu\frac{\partial}{\partial x_j}\left(\frac{\partial\langle\rho U_i\rangle}{\partial x_j} + \frac{\partial\langle\rho U_j\rangle}{\partial x_i}\right) + \rho\frac{\partial\tau_{ij}}{\partial x_j} \tag{5}$$

Here, $U_i$ denotes the velocity components, $P$ is the static pressure, $\nu$ is the kinematic viscosity, $\rho$ is the density, and $\mathrm{D}/\mathrm{D}t$ is the material derivative. The subscripts $l$ and $v$ indicate liquid and vapor, respectively, while symbols without subscript refer to the mixture. Furthermore, $\dot{m}$ is the source term due to the cavitation model (see Sec. 3.3), and $\tau_{ij}$ denotes the Reynolds stress tensor, which is computed according to

$$\tau_{ij} \cong 2\nu_t\langle S_{ij}\rangle - \frac{2}{3}k\delta_{ij} - a_{ij}k \tag{6}$$

where $\nu_t$ denotes the eddy viscosity, $S_{ij}$ is the strain rate tensor, $k$ is the turbulence kinetic energy, $\delta_{ij}$ is the Kronecker delta, and $a_{ij}$ is the anisotropic part of the Reynolds stress tensor. For the SST, KSKL, DDES, and IDDES models, $a_{ij} = 0$, such that Eq. (6) reduces to the Boussinesq's hypothesis.

**3.1 Turbulence Models.** The turbulence models applied in this work are divided into commonly used two-equation RANS approaches (SST and KSKL), approaches which model the anisotropic Reynolds stress tensor (explicit algebraic Reynolds stress model (EARSM) and RSM) and scale resolving simulation (DDES and IDDES). For all models, the main equations are given.

*3.1.1 $k-\omega$ Shear Stress Transport.* The $k-\omega$ SST model [18] is a blending between $k-\omega$ and $k-\epsilon$ models and is widely used for industrial applications. The model consists of a transport equation for the turbulence kinetic energy ($k$) and specific dissipation rate ($\omega$)

$$\frac{\mathrm{D}k}{\mathrm{D}t} = P_k - \beta^*\omega k + \frac{\partial}{\partial x_j}\left[(\nu + \sigma_k\nu_t)\frac{\partial k}{\partial x_j}\right] \tag{7}$$

$$\frac{\mathrm{D}\omega}{\mathrm{D}t} = \frac{\alpha}{\nu_t}P_k - \beta\omega^2 + \frac{\partial}{\partial x_j}\left[(\nu + \sigma_\omega\nu_t)\frac{\partial\omega}{\partial x_j}\right] + 2(1-F_1)\frac{\sigma_{\omega,2}}{\omega}\frac{\partial k}{\partial x_j}\frac{\partial\omega}{\partial x_j} \tag{8}$$

The production of $k$ and eddy viscosity are modeled as

$$P_k = \min\left(\nu_t\langle S\rangle^2, 10\beta^*k\omega\right) \quad \text{and} \quad \nu_t = \frac{a_1 k}{\max(a_1\omega, \langle S\rangle)F_2} \tag{9}$$

respectively. Here, $\langle S\rangle = \sqrt{2S_{ij}S_{ij}}$ is the magnitude of the strain rate tensor. The blending functions, $F_1$ and $F_2$, as well as the model constants $\alpha$, $\beta^*$, $\sigma_k$, $\gamma$, $\beta$, $\sigma_\omega$, and $\sigma_{\omega,2}$ are defined by Ref. [18].

*3.1.2 $k-\sqrt{k}L$.* The KSKL model [19] introduces an additional length scale, the von Karman length scale ($L_{vK}$), and exhibits a reduced eddy viscosity. The model is also accompanied by improved iterative convergence compared to the SST model. The transport equations are defined as

$$\frac{\mathrm{D}k}{\mathrm{D}t} = \nu_t\langle S\rangle^2 - C_\mu^{3/4}\frac{k^{3/2}}{L} + \frac{\partial}{\partial x_j}\left[\left(\nu + \frac{\nu_t}{\sigma_k}\right)\frac{\partial k}{\partial x_j}\right] - 2\nu\frac{k}{d_w^2} \tag{10}$$

$$\frac{\mathrm{D}\sqrt{k}L}{\mathrm{D}t} = \frac{\sqrt{k}L}{k}\nu_t\langle S\rangle^2\left(\zeta_1 - \zeta_2\left(\frac{L}{L_{\nu k}}\right)^2\right) - \zeta_3 k + \frac{\partial}{\partial x_j}\left[\left(\nu + \frac{\nu_t}{\sigma_{\sqrt{k}L}}\right)\frac{\partial(\sqrt{k}L)}{\partial x_j}\right] - 6\nu\frac{\sqrt{k}L}{d_w^2}f_{\sqrt{k}L} \tag{11}$$

with $d_w$ denoting the distance to the closest wall, and $f_{\sqrt{k}L}$ acting as a viscous sublayer model [19]. In these equations, the eddy viscosity and von Karman length scale are defined as

$$\nu_t = C_\mu^{1/4}\frac{kL}{\sqrt{k}} \quad \text{and} \quad L_{vK} = \kappa\frac{|U'|}{|U''|} \tag{12}$$

with $\kappa$ being the von Karman constant and

$$|U'| = \sqrt{\frac{\partial\langle U_i\rangle}{\partial x_j}\frac{\partial\langle U_i\rangle}{\partial x_j}} \quad \text{and} \quad |U''|\sqrt{\frac{\partial^2\langle U_i\rangle}{\partial x_j\partial x_j}\frac{\partial^2\langle U_i\rangle}{\partial x_k\partial x_k}} \tag{13}$$

For the model constants $C_\mu$, $\zeta_1$, $\zeta_2$, $\zeta_3$, $\sigma_{\sqrt{k}L}$ and function $f_{\sqrt{k}L}$, see Ref. [19].

*3.1.3 Explicit Algebraic Reynolds Stress Model.* The EARSM [20], in addition to solving the transport equations for $k$ and $\omega$, models the anisotropic part of the Reynolds stress tensor $a_{ij}$, resulting in a nonlinear constitutive relation between the Reynolds stress tensor and the filtered velocity gradients (see Eq. (6)). The anisotropic part is modeled by a tensor polynomial

$$\begin{aligned} a_{ij} = {} & \beta_3\left(\langle\Omega_{ik}^*\rangle\langle\Omega_{kj}^*\rangle - \frac{1}{3}\langle II_\Omega\rangle\delta_{ij}\right) + \beta_4\left(\langle S_{ik}^*\rangle\langle\Omega_{kj}^*\rangle - \langle\Omega_{ik}^*\rangle\langle S_{kj}^*\rangle\right) \\ & + \beta_6\left(\langle S_{ik}^*\rangle\langle\Omega_{kl}^*\rangle\langle\Omega_{lj}^*\rangle + \langle\Omega_{ik}^*\rangle\langle\Omega_{kl}^*\rangle\langle S_{lj}^*\rangle - \langle II_\Omega\rangle\langle S_{ij}^*\rangle - \frac{2}{3}\langle IV\rangle\delta_{ij}\right) \\ & + \beta_9\left(\langle\Omega_{ik}^*\rangle\langle S_{kl}^*\rangle\langle\Omega_{lm}^*\rangle\langle\Omega_{mj}^*\rangle - \langle\Omega_{ik}^*\rangle\langle\Omega_{kl}^*\rangle\langle S_{lm}^*\rangle\langle\Omega_{mj}^*\rangle\right) \end{aligned} \tag{14}$$

in which the strain rate and vorticity tensors are included in nondimensional form

$$\langle S_{ij}^*\rangle = \frac{1}{2\beta^*\omega}\left(\frac{\partial\langle U_i\rangle}{\partial x_j} + \frac{\partial\langle U_j\rangle}{\partial x_i}\right) \tag{15}$$

$$\langle\Omega_{ij}^*\rangle = \frac{1}{2\beta^*\omega}\left(\frac{\partial\langle U_i\rangle}{\partial x_j} - \frac{\partial\langle U_j\rangle}{\partial x_i}\right) \tag{16}$$

respectively. The transport equations for $k$ and $\omega$ are given by Eqs. (7) and (8), respectively, with Eq. (9) being modified as follows:

$$P_k = \nu_t\langle S\rangle^2 \quad \text{and} \quad \nu_t = \frac{C_\mu}{\beta^*}\frac{k}{\omega} \tag{17}$$

The $\beta$-coefficients are a function of the three independent invariants of the tensors $II_\Omega$ and $IV$ (for details on these formulations and $C_\mu$, the reader is referred to Ref. [20]). This work employs the calibration constants of Ref. [29].

*3.1.4 Reynolds Stress Model.* Instead of modeling the Reynolds stress tensor according to the Boussinesq hypothesis, the RSM [21] determines all components of the Reynolds stress tensor separately. This is done by solving a transport equation for each of them, which can be written as

$$\frac{\mathrm{D}R_{ij}}{\mathrm{D}t} = P_{ij} + \Pi_{ij} + \varepsilon_{ij} + D_{ij} \tag{18}$$

with $R_{ij} = -\tau_{ij}/\rho$. In Eq. (18), $P_{ij}$ denotes production of the Reynolds stresses

$$P_{ij} = -\tau_{ik}\frac{\partial\langle U_j\rangle}{\partial x_k} - \tau_{jk}\frac{\partial\langle U_i\rangle}{\partial x_k} \tag{19}$$

$\Pi_{ij}$ the pressure strain correlation term

$$\Pi_{ij} = -\left(\beta^* C_1 k\omega + \frac{1}{2} C_1^* P_{kk}\right) a_{ij} + \beta^* C_2 k\omega \left(a_{ik}a_{kj} - \frac{1}{3} a_{kl}a_{kl}\delta_{ij}\right) + \left(C_3 - C_3^* \sqrt{a_{kl}a_{kl}}\right) k\langle S_{ij}\rangle + C_5 k\left(a_{ik}\langle \Omega_{jk}\rangle + a_{jk}\langle \Omega_{ik}\rangle\right) + C_4 k\left(a_{ik}\langle S_{jk}\rangle + a_{jk}\langle S_{ik}\rangle - \frac{2}{3} a_{kl}\langle S_{kl}\rangle \delta_{ij}\right) \tag{20}$$

$\varepsilon_{ij}$ the dissipation of $\tau_{ij}$

$$\varepsilon_{ij} = \frac{2}{3}\beta^* k\omega \delta_{ij} \quad \text{with} \quad k = \frac{1}{2}\tau_{ii} \tag{21}$$

and $D_{ij}$ the diffusion term

$$D_{ij} = \frac{\partial}{\partial x_j}\left[\left(\nu + \nu_t \frac{C_6}{\beta^*}\right)\frac{\partial \tau_{ij}}{\partial x_j}\right] \tag{22}$$

The specific dissipation $\omega$ is determined using Eq. (8), but with $P_{kk}$ instead of $P_k$. The values of constants $a$, $\beta$, and $C$ are given by Ref. [21].

*3.1.5 Delayed Detached-Eddy Simulation.* The hybrid models employed in this work rely on applying RANS and LES in a zonal manner. Both models applied use the SST model in the RANS region and as a subfilter model in the LES region. The coupling with the LES region is achieved by modifying Eq. (7) to

$$\frac{\mathrm{D}k}{\mathrm{D}t} = P_k - \frac{\sqrt{k^3}}{l_t} + \frac{\partial}{\partial x_j}\left[(\nu + \sigma_k \nu_t)\frac{\partial k}{\partial x_j}\right] \tag{23}$$

The inclusion of the turbulent length $l_t$ reduces the eddy viscosity in LES regions, allowing instabilities to develop, and is a function of the RANS length scale

$$l_t^{\mathrm{RANS}} = \sqrt{k}/(C_\mu \omega) \tag{24}$$

and the LES length scale

$$l_t^{\mathrm{LES}} = C_{\mathrm{LES}1} F_1 \Delta_c + C_{\mathrm{LES}2}(1 - F_1)\Delta_c \tag{25}$$

In these equations, $\Delta_c$ denotes the maximum edge length of the grid cell and $F_1$ the blending function of the SST model.

In DDES, the entire boundary layer is solved using RANS. Following Ref. [22], the length scale is defined as

$$l_t^{\mathrm{DDES}} = l_{\mathrm{RANS}} - \tilde{f}_d \max(0, l_{\mathrm{RANS}} - l_{\mathrm{LES}}) \tag{26}$$

The auxiliary function $\tilde{f}_d$ is defined in Ref. [22].

*3.1.6 Improved Delayed Detached-Eddy Simulation.* In order to improve the accuracy of the DDES model near the wall, IDDES [23] also applies LES in the outer part of the boundary layer, where the resolution is sufficient. The model relies on a different formulation for the length scale

$$l_t^{\mathrm{IDDES}} = \tilde{f}_d(1 + f_e) l_t^{\mathrm{RANS}} + (1 - \tilde{f}_d) l_t^{\mathrm{LES}} \tag{27}$$

Auxilliary functions $\tilde{f}_d$ and $f_e$ can be found in Ref. [23]; calibration constants are published by Ref. [30].

**3.2 Transition Model.** The LCTM [31] uses the intermittency ($\gamma$) to modify the turbulence kinetic energy production ($P_k$) and destruction ($D_k$) terms of the SST turbulence model

$$\tilde{P}_k = \gamma_{\mathrm{eff}} P_k \quad \text{and} \quad \tilde{D}_k = \min[\max(\gamma_{\mathrm{eff}}, 0.1)] \tag{28}$$

where $\gamma_{\mathrm{eff}} = \max(\gamma, \gamma_{\mathrm{sep}})$. Here, $\gamma_{\mathrm{sep}}$ is a modification to the intermittency for predicting separation-induced transition. The transport equation for the intermittency reads

$$\frac{\mathrm{D}\gamma}{\mathrm{D}t} = P_\gamma - E_\gamma + \frac{\partial}{\partial x_j}\left[(\nu + \nu_t)\frac{\partial \gamma}{\partial x_j}\right] \tag{29}$$

At the start of the boundary layer, $\gamma = 0$, which corresponds to a completely laminar flow. As the boundary layer develops, the intermittency is mainly increased by the production term

$$P_\gamma = F_{\mathrm{length}} C_{a1} |\langle S_{ij}\rangle| [\gamma F_{\mathrm{onset}}]^{0.5} (1 - C_{e1}\gamma) \tag{30}$$

In Eq. (30), $F_{\mathrm{length}}$ determines the transition length and the limiter $F_{\mathrm{onset}}$ ensures that $P_\gamma$ is zero upstream of the transition point and is activated when transition starts. The transition Reynolds number in the freestream is determined using the turbulence intensity and pressure gradient, i.e., $\mathrm{Re}_{\theta_t} = f(I, \partial p/\partial x_i)$. The global quantity $\mathrm{Re}_{\theta_t}$ is translated to a local quantity $\tilde{R}e_{\theta_t}$ in the boundary layer by means of the transport equation

$$\frac{\mathrm{D}\tilde{R}e_{\theta t}}{\mathrm{D}t} = P_{\theta t} + \frac{\partial}{\partial x_j}\left[\sigma_{\theta t}(\nu + \nu_t)\frac{\partial \tilde{R}e_{\theta t}}{\partial x_j}\right] \tag{31}$$

Information from the freestream is relayed into the boundary layer by means of the diffusion term. When $\tilde{R}e_{\theta_t}$ exceeds the critical Reynolds number, $\gamma$ increases. In order to match the local and global variables in the freestream, a production term is employed

$$P_{\theta t} = \frac{C_{\theta_t} U_\infty^2}{500\nu}\left(\mathrm{Re}_{\theta t} - \tilde{R}e_{\theta t}\right)(1.0 - F_{\theta t}) \tag{32}$$

The blending factor $F_{\theta_t}$ is responsible for deactivating production inside the boundary layer and activating the term in the freestream. For the definition of $\gamma_{\mathrm{sep}}$, $F_{\mathrm{length}}$, $F_{\mathrm{onset}}$, and $F_{\theta_t}$ see Ref. [31].

**3.3 Cavitation Model.** In cavitating conditions, the multiphase flow is modeled using the homogeneous mixture Eulerian volume of fluid (VoF) approach [32]. An additional transport equation is solved for the vapor volume fraction, $\alpha_v = \mathcal{V}_v/(\mathcal{V}_v + \mathcal{V}_l)$, with $\mathcal{V}$ indicating the phase volume. The transport equation is formulated as

$$\frac{\mathrm{D}\alpha_v}{\mathrm{D}t} = \frac{\dot{m}}{\rho_v} \tag{33}$$

From $\alpha_v$, the mixture properties can be calculated using

$$\rho = \alpha_v \rho_v + (1 - \alpha_v)\rho_l \quad \text{and} \quad \nu = \alpha_v \nu_v + (1 - \alpha_v)\nu_l \tag{34}$$

under the condition that

$$\alpha_l + \alpha_v = 1 \tag{35}$$

The source term $\dot{m}$ also appears in the continuity equation (Eq. (4)), and is modeled by the Schnerr–Sauer cavitation model [33], which is based on the Rayleigh–Plesset equation for bubble dynamics and reads

$$\frac{\dot{m}}{\rho_v} = \begin{cases} 4\pi R_B^2 n_b (1 - \alpha_v)\sqrt{\dfrac{2}{3}\dfrac{|p_v - p|}{\rho_l}}, & \text{if } p < p_v \\ -\dfrac{3\alpha_v}{R_B}\sqrt{\dfrac{2}{3}\dfrac{|p_v - p|}{\rho_l}}, & \text{if } p > p_v \end{cases} \tag{36}$$

$R_B$ indicates the maximum bubble radius, $n_b$ the bubble concentration, and $p_v$ the vapor pressure.

## 4 Error Analysis

**4.1 Numerical Errors.** The process of solving differential equations numerically gives rise to numerical errors. The total numerical error $E_n$ of a variable $\varphi$ can be decomposed in

$$E_n(\varphi) \equiv \varphi - \varphi_0 = E_r(\varphi) + E_{it}(\varphi) + E_d(\varphi) + E_s(\varphi) \tag{37}$$

where $\varphi_0$ denotes the exact numerical solution, $E_r(\varphi)$ the round-off error, $E_{it}(\varphi)$ the iterative error, $E_d(\varphi)$ the discretization error, and $E_s(\varphi)$ the statistical error. The numerical uncertainty $U_n(\varphi)$ consists of the same components given in Eq. (37).

In this work, all computations were run with double-precision leading to a negligible round-off error. A (case dependent) convergence criterion was set, to ensure an iterative error of at least one order of magnitude below the discretization error. For more details, the reader is referred to Ref. [34]. The spatial, and temporal (in the case of unsteady calculations), discretization errors were determined by a systematic refinement study [35]. This method relies on a (truncated) power series expansion

$$E_d(\varphi) \approx \beta_s(h_i/h_1)^{q_s} + \beta_t(t_i/t_1)^{q_t} \tag{38}$$

where $h_i/h_1$ and $t_i/t_1$ are the spatial (grid) and temporal (timestep) refinement levels, the indices $s$ and $t$ the spatial and temporal components, $\beta$ the constants to be determined, and $q$ the observed orders of grid convergence. To increase robustness, $q$ and $\beta$ are determined using a least-square fitting requiring at least four grids and four timesteps for time-resolved simulations, and four grids for steady simulations. This error is translated to a discretization uncertainty $U_d(\varphi)$ as reported by Ref. [35].

The statistical error is a result of the finite simulated physical time, and the dependency of the result on the initial conditions. To address both simultaneously, the transient scanning technique is used, in which the standard deviation of the time signal is compared to the theoretically expected trend for a stochastic stationary process in order to determine how many timesteps can be used for calculating flow statistics and the associated statistical uncertainty [36].

**4.2 Modeling Error.** The modeling error was determined by comparing the results against the S-PIV measurements by Ref. [10]. Vortex wandering was accounted for in the analysis of this dataset by using the correlation conditional weighted temporal average. Validation was performed at the closest available measurement location to the tip ($x/c_0 = 0.50$). The Reynolds number was not matched exactly since the inflow velocity in the measurement facility was set with a precision of 0.5% [10]. Arndt and Keller [37] showed that the effect this has on the integral quantities is negligible.

Validation of velocity distributions was based on the multivariate metric, which allows the modeling error to be determined based on an arbitrary set of data points [38]. The metric $r$ is dependent on the modeling error, defined as the difference between the simulation and the experiment, $E_m = \varphi - \varphi_e$, and the validation uncertainty, which is the sum of the numerical and experimental uncertainties, $U_v(\varphi) = U_n(\varphi) + U_e(\varphi)$. For $N_p$ points, the metric reads

$$r = \sqrt{\mathbf{E}_m^T \mathbf{U}_v^{-1} \mathbf{E}_m} \tag{39}$$

with

$$\mathbf{E}_m = [E_{m,N_1}, \ldots, E_{m,N_p}]^{\mathrm{T}} \tag{40}$$

and

$$\mathbf{U}_v = \mathrm{diag}([U_{v,N_1}, \ldots, U_{v,N_p}]) \tag{41}$$

If the uncertainties in the points are represented by a normal distribution, the expected value of $r$ is represented by a $\chi^2-$ distribution. This means that the reference value $r_{\mathrm{ref}}$ is the sum of the expected value and the standard uncertainty [39]

$$r_{\mathrm{ref}} = \sqrt{N_p + \sqrt{2N_p}} \tag{42}$$

When $r/r_{\mathrm{ref}}$ exceeds 1.0, the modeling error is globally higher than the validation uncertainty. If $r/r_{\mathrm{ref}} \leq 1$, the difference between experimental data and numerical results is within the level of $U_v(\varphi)$, which indicates that the model is valid.

With respect to transition behavior, the best reference material of the flow over the surface of the wing is flow visualization of the suction side [37,40]. No quantitative measurements of the boundary layer flow over the wing were found in literature meaning that the modeling error for the transition simulations in Sec. 6 could not be assessed.

## 5 Numerical Setup

**5.1 Solver.** Computations were performed using ReFRESCO [41], which is a community-based open-usage/open-source CFD code for the maritime world. It computes multiphase unsteady incompressible viscous flows using the Navier–Stokes equations, complemented with turbulence and cavitation models. The equations are discretized using the finite volume approach with cell-centered collocated variables, in strong-conservation form, with a pressure-correction equation based on the SIMPLE algorithm used to ensure mass conservation. Time integration was performed implicitly by a second-order scheme. The gradients in all diffusion terms were calculated using Gauss' theorem and interpolated to the cell faces by central differencing, which results in second-order accuracy. For the discretization of the convective terms, the second-order accurate quadratic upstream interpolation for convective kinematics (QUICK) scheme was used. For robustness reasons, the convective terms of the LCTM were discretized by means of a first-order upwind scheme [42].

**5.2 Computational Domain.** The "Arndt" wing is an elliptical planform with a NACA $66_2 - 415$ cross section, a root chord of $c_0 = 0.1256$ m (4.9449 in.), a wingspan of $b = 0.15$ m (5.91 in.) and an area of $A = 0.01465$ m$^2$ (22.7 in.$^2$). The computational domain corresponds to the cavitation tunnel used in the experiments by Pennings et al. [10], with an inlet located $5c_0$ upstream of the wing and an outlet located $10c_0$ downstream. The domain is visualized in Fig. 2.

The domain topology consists of multiblock hexahedral structured grids, with additional refinement around the wing's edges. To minimize numerical diffusion, *a priori* grid refinement was employed to increase the resolution in the vortex and wake regions [43]. For the resolution in the vortex, the recommendations by Asnaghi et al. [44] of an in-plane and streamwise resolution of $\eta_v/8$ and $\eta_v/4$ were met for the finest grid. For the wake

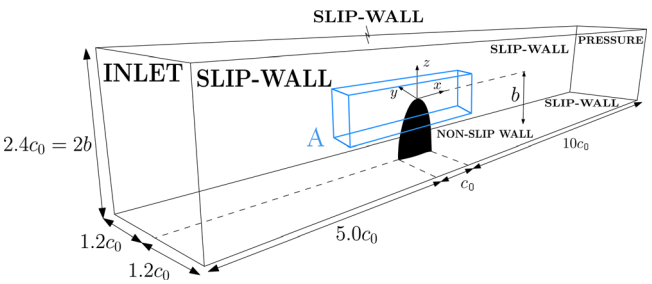


**Fig. 2 Computational domain including dimensions normalized by $c_0$, and boundary conditions. The grid topology in the blue box, designated A, is shown in Fig. 3.**

**Table 1 Details of the geometrically similar grids for the wing at $\alpha = 5$ deg and 9 deg**

| | $N_c/10^6$ | | $h_i/h_1$ | | $\overline{x_n^+} \times 10^1$ | | $\overline{x_c^+}/10^2$ | | $\overline{x_s^+}/10^3$ | |
|---|---|---|---|---|---|---|---|---|---|---|
| Grid | 5 deg | 9 deg | 5 deg | 9 deg | 5 deg | 9 deg | 5 deg | 9 deg | 5 deg | 9 deg |
| $G_{1,\alpha}$ | 5.72 | 6.59 | 1.00 | 1.00 | 1.17 | 1.25 | 2.65 | 2.71 | 0.53 | 0.61 |
| $G_{2,\alpha}$ | 2.69 | 3.11 | 1.28 | 1.28 | 1.47 | 1.55 | 3.43 | 3.51 | 0.69 | 0.79 |
| $G_{3,\alpha}$ | 1.40 | 1.61 | 1.59 | 1.59 | 1.85 | 1.96 | 4.26 | 4.36 | 0.86 | 0.98 |
| $G_{4,\alpha}$ | 0.63 | 0.73 | 2.08 | 2.08 | 2.39 | 2.53 | 5.67 | 5.82 | 1.14 | 1.30 |

Note: Surface averaged ($\bar{\cdot}$) nondimensional normal ($n$), chordwise ($c$), and spanwise ($s$) wall cell sizes obtained from steady $k-\omega$ SST simulations.

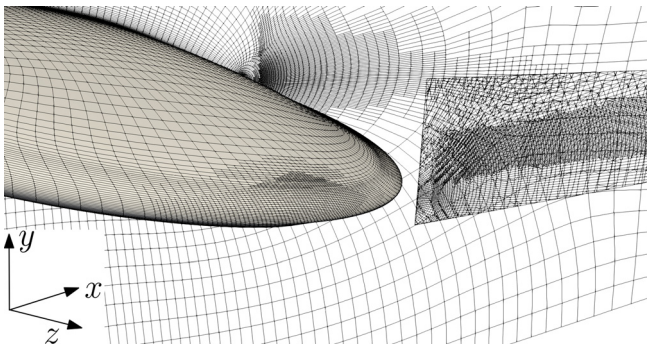


**Fig. 3 Visualization of the wing surface grid, the wake region, and the vortex region indicated by box A in Fig. 2**

region, a sensitivity analysis of the vortex variables to the refinement levels in the wake region was carried out [42]. Table 1 presents the grid details and nondimensional wall cell sizes on the wing surface for both 5 and 9 deg AoA. Figure 3 visualizes the grid topology at the wall, wing's surface and in the wake region.

**5.3 Computational Setup.** The most widely considered test condition in literature is for a root chord-based Reynolds number of $8.95 \times 10^5$. Using $\nu = 1.002 \times 10^{-6}\text{m}^2/\text{s}$ (1.002 cSt) and $\rho = 998\,\text{kg/m}^3$ (8.33 lb/gal), this yields an inflow velocity of $U_\infty = 7.15$ m/s (23.5 ft/s).

The convergence criterion for all variables was set to be at least $10^{-5}$ for the maximum residuals ($L_\infty$), normalized by the diagonal element of the left-hand-side matrix of the linear system of equations. This ensures that the iterative error was at least one order of magnitude lower than the discretization error ($\mathcal{O}(1)\%$). The discretization error was determined using timesteps $[\Delta t_1, \Delta t_2, \Delta t_3, \Delta t_4] \times U_\infty/c_0 = [1.09, 1.41, 1.75, 2.27] \times 10^{-2}$ to ensure that the Courant number in the LES regions of the hybrid models was less than one in the vortex for the finest grid-timestep combination.

In cavitating conditions, simulations were run for a cavitation number

$$\sigma = \frac{p_\infty - p_v}{1/2\rho U_\infty^2} \tag{43}$$

of 1.6 to obtain tip vortex cavitation, while avoiding sheet cavitation [11]. Although the specified number of seeds and bubble radius are expected to affect the liquid–vapor interface, their effect was considered to be out of the scope of this research. These were set to $n_b = 1 \times 10^9$ and $R_B = 3 \times 10^{-5}$ m ($1.2 \times 10^{-4}$ in.), respectively, based on Refs. [11], [33], and [41].

The boundary conditions at the inlet are a Dirichlet condition for all velocity components and turbulence quantities, and at the outlet a Dirichlet condition for the pressure. The wing's surface was modeled as a nonslip wall, the other domain boundaries were modeled as slip walls. At the inflow a turbulence intensity of $I = 1.0\%$ and an eddy viscosity ratio $\nu_t/\nu = 1.0$ are prescribed, unless mentioned otherwise.

## 6 Effect of Transition Modeling

To demonstrate numerically that the fully turbulent boundary layer assumption is invalid for this test case and contributes to the underpredicted cavity sizes as published in literature, the LCTM model is applied. The SST turbulence model was used, since in ReFRESCO the LCTM is only compatible with this model.

The numerical settings were based on Ref. [42]. In that work, it was shown that the transition location on the suction side for $\alpha = 5$ deg is sensitive to the turbulent inflow conditions, while for $\alpha = 9$ deg, transition on the suction side is triggered just downstream of the leading edge (LE) regardless of the inflow conditions. To obtain this sensitivity at $\alpha = 5$ deg, the eddy viscosity ratio ($\nu_t/\nu$) and turbulence intensity ($I$) should be varied simultaneously. In order to avoid problems with excessive decay of turbulence in the freestream, the turbulence quantities are frozen until $0.1c_0$ upstream of the LE. To vary the boundary layer thickness of the wing on the suction side, turbulence intensities of $I = 0.5$, 1.0, 2.0, and 4.0% and eddy viscosity ratios of $\nu_t/\nu = 0.5$, 1.0, 2.0, and 4.0 were used. In the remainder of this document these combinations will be denoted as $[I/\%, \nu_t/\nu]$.

Only steady computations were performed since no unsteady flow features around the surface of the wing were observed in literature, both numerically [11–13] and experimentally [14,40]. Section 6.1 relates the state of the boundary layer to the vortex in wetted flow conditions, while Sec. 6.2 investigates the effect of transition modeling on cavitating flow.

**6.1 Boundary Layer—Vortex Interaction in Wetted Flow.** First, the relationship given in Eq. (1) is tested, i.e., $\delta_s \propto \text{Re}_c^h$. Figure 4 displays the suction side of the wing with the limiting streamlines for both AoA. The surface is colored by the magnitude of the wall shear stress. The SST simulations clearly yield a turbulent boundary layer over the entire wing. Applying the transition model for $[I/\%, \nu_t/\nu] = 4.0$ results in natural transition at $x_{LE}/c_0 \approx 0.4$ along the wing, and separation induced transition near the tip for $\alpha = 5$ deg. Based on a visual comparison, the limiting streamlines predicted by the transition model with $[I/\%, \nu_t/\nu] = 1.0$ and 0.5 are closest to the experimental visualizations by Refs. [37] and [40]. For the wing at 9 deg the boundary layer is mostly turbulent for all inflow conditions. Decreasing the turbulent inflow conditions increases the amount of laminar flow for $\alpha = 9$ deg, but this change is much less compared to $\alpha = 5$ deg. In order to quantify the change in boundary layer thickness, Fig. 5 shows the boundary layer thickness along the chord at half-span. It is clear that lower values of the inflow turbulence quantities result in a smaller $\delta_s$. The boundary layer thickness for the wing at 5 deg is more sensitive to the turbulent inflow conditions compared to $\alpha = 9$ deg: for the most laminar boundary layer compared to the fully turbulent boundary layer, $\delta_s$ is decreased by a factor of 3.0 and 1.2, respectively. When this information is used in connection with Eq. (1), the difference in $h$ for the fully turbulent and most laminar boundary layer is approximately 0.1,

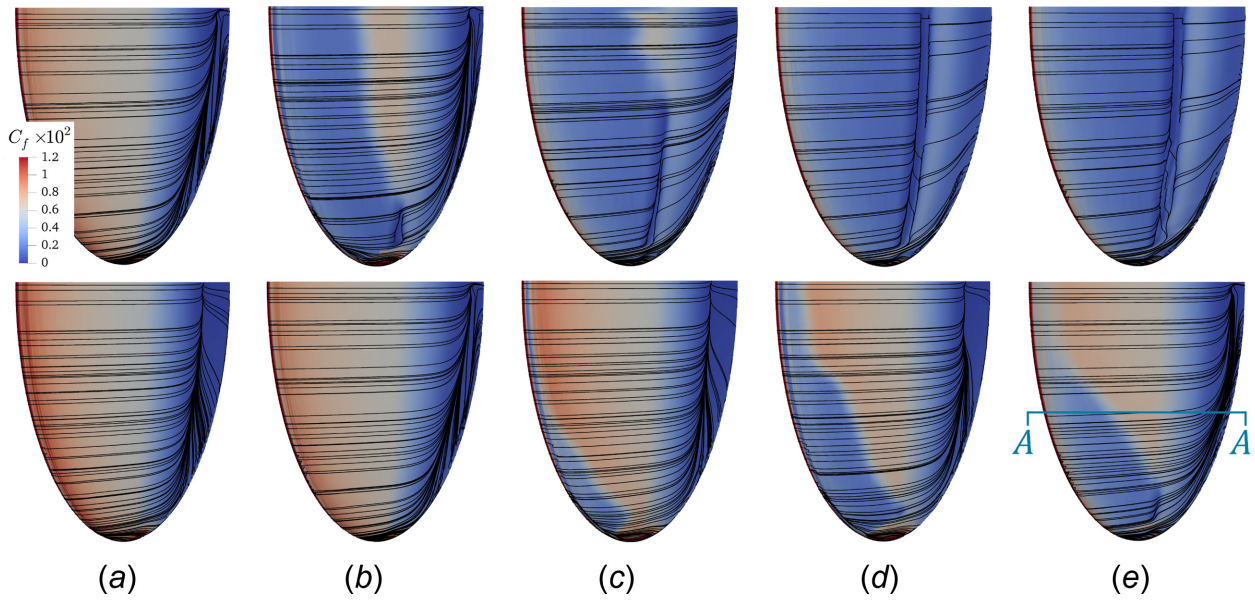


**Fig. 4 Limiting streamlines over the suction side of the wing at $\alpha = 5$ deg (top row) and $\alpha = 9$ deg (bottom row) predicted by the SST and LCTM with different turbulence inflow conditions. The surface is colored by the skin friction coefficient ($C_f = |\tau_{w,x}|/(1/2\rho U_\infty^2)$). In (*e*) cross section A-A, located at $z/b = 0.5$, is indicated. (*a*) SST, (*b*) $[I/\%, \nu_t/\nu] = 4.0$, (*c*) $[I/\%, \nu_t/\nu] = 2.0$, (*d*) $[I/\%, \nu_t/\nu] = 1.0$, and (*e*) $[I/\%, \nu_t/\nu] = 0.5$.**

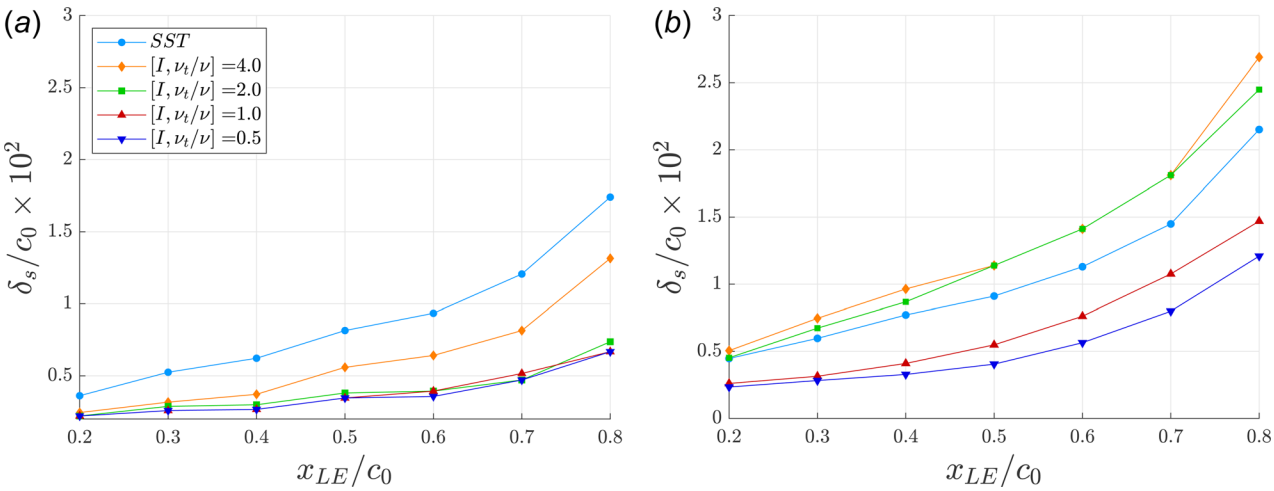


**Fig. 5 Boundary layer thickness along the chord at section A-A (see Fig. 4(*e*)) for wetted flow conditions. (*a*) $\alpha = 5$ deg (*b*) $\alpha = 9$ deg.**

which is in the same order of magnitude as the difference given for flat plates by McCormick [25].

The effect of the sensitivity of the boundary layer thickness to the turbulent inflow conditions on the pressure in the vortex is considered next. This is the relationship given in Eq. (3), i.e., $p(\eta = 0) \propto \eta_v$ and $\Gamma_0 \propto \delta_s$. Figure 6 shows the effect of the change in $\delta_s$ on the vortex core radius and the wing's circulation relative to the fully turbulent boundary layer for both AoA. For $\alpha = 5$ deg, the decrease in boundary layer thickness translates into an average reduction of $\eta_v$ of 7% over the considered trajectory and an increased circulation of 3.7%. For the wing at 9 deg these differences become 1% and 6.2%, respectively.

Figure 7 presents the effect of the change in $\eta_v$ and $\Gamma_0$, and so indirectly of $\delta_s$, on the pressure in the center of the vortex. For the wing at 5 deg the pressure in the vortex center is reduced by 20%. For $\alpha = 9$ deg, the reduction is 7%. This confirms the hypothesis and shows that the fully turbulent boundary layer assumption is not valid for $\alpha = 5$ deg. It can yield an input uncertainty of 20% if the numerical results are compared to experimental results in which the transition location is not controlled or measured. For 9 deg this input error is smaller since transition is triggered near the LE regardless of the turbulent inflow conditions.

Referring to Eq. (2), the pressure coefficient is dependent on $1/\eta_v^2$ and $\Gamma_0^2$. Figure 7 displays the cumulative effect of both factors by the dashed line, i.e.,

$$\frac{(C_p)_{\eta=0,\text{expected}}}{(C_p)_{\eta=0,\text{SST}}} = \frac{1/\eta_v^2}{(1/\eta_v^2)_{\text{SST}}} \frac{\Gamma_0^2}{(\Gamma_0^2)_{\text{SST}}} \tag{44}$$

It can be seen that this expected decrease in $C_p$ agrees well with the actual decrease in the simulations (solid lines), showing that the CFD results agree with the proportionality of the semi-

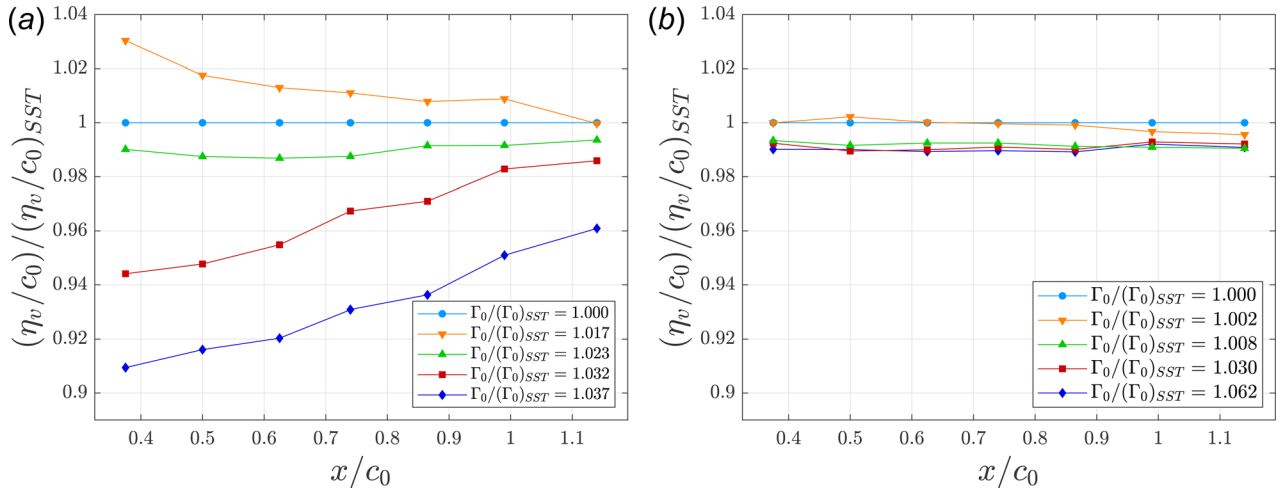


**Fig. 6 Vortex core radius along the vortex trajectory, and wing circulation, predicted by the transition model for wetted flow conditions. All results are normalized with respect to a fully turbulent boundary layer (SST result) and line styles correspond to the legend of Fig. 5. (*a*) $\alpha = 5$ deg (*b*) $\alpha = 9$ deg.**

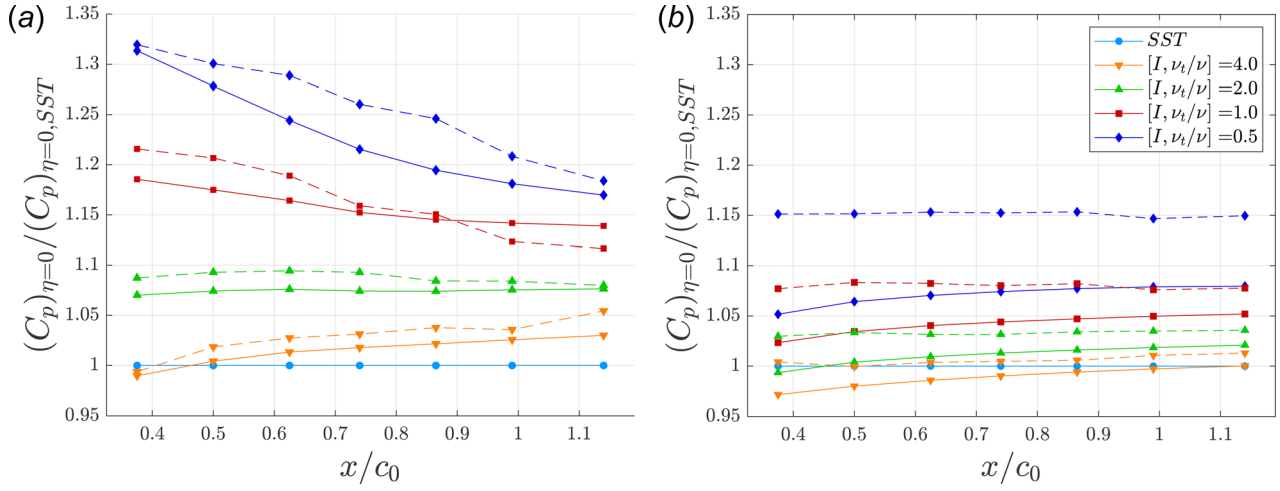


**Fig. 7 Pressure coefficient of the simulations with transition model (solid lines) and expected $(C_p)_{\eta=0}$ based on $1/\eta_v^2$ and $\Gamma_0^2$ (dashed lines) in the vortex center along the vortex trajectory for wetted flow conditions. All results are normalized with respect to a fully turbulent boundary layer (SST result). (*a*) $\alpha = 5$ deg (*b*) $\alpha = 9$ deg.**

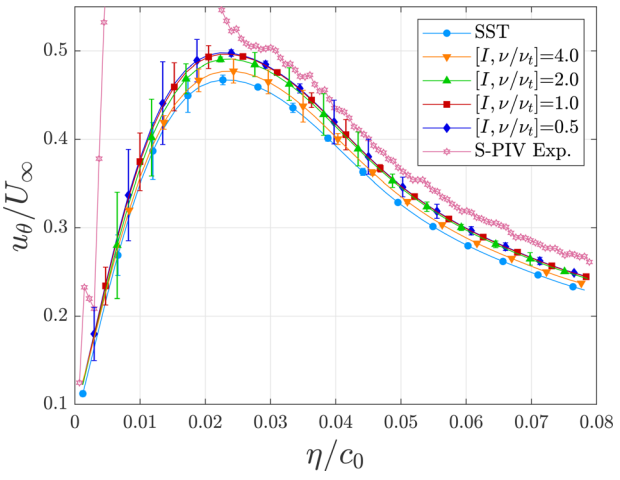


**Fig. 8 Azimuthal velocity profiles predicted by the transition model at $x/c_0 = 0.50$ and $\alpha = 5$ *deg* for wetted flow conditions. The S-PIV measurements are obtained by Ref. [10].**

analytical expression. Near the wing (i.e., for $x/c_0 < 1.0$), the proportionality consistently overpredicts the change in $(C_p)_{\eta=0}$ because the roll-up process is not yet finished, and incorporating the full effect of the change in $\Gamma_0$ is not valid (see Sec. 2). One exception is the $\alpha = 9$ deg, $[I/\%, \nu_t/\nu] = 0.5$ case which overestimates the change in $(C_p)_{\eta=0}$. For this computation, the predicted wing circulation increases due to separation induced transition, which prevents the flow from separating later near the trailing edge of the wing.

Figure 8 compares the circumferentially averaged azimuthal velocity profile within the vortex in sector I for $\alpha = 5$ deg. Sector I designates the top quarter of the vortex (in positive lift direction) since [10] illuminated the suction side of the wing, leading to less reliable measurements in the bottom quarter (in negative lift direction). It is observed that for $\eta/c_0 > 0.025$ applying the transition model decreases the modeling error and that the lines converge toward the experimental result as the boundary layer thickness reduces. However, the figure highlights the limitation of the SST turbulence model for accurately predicting vortical flows, especially for $\eta/c_0 < 0.025$ where the experimental results show a significantly higher azimuthal velocity.

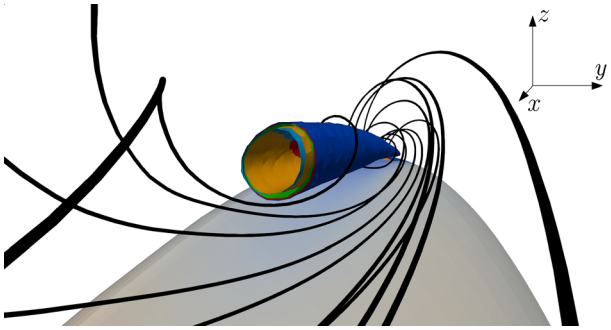


**Fig. 9 Isocontours of the vapor volume fraction ($\alpha_v = 0.1$) for the SST and LCTM simulations with streamlines. Cavities are clipped to reveal their cross section. Colors are according the legend of Fig. 8.**

**6.2 Boundary Layer—Vortex Interaction in Cavitating Flow.** In cavitating flow conditions, the wing is only considered at 5 deg to maximize the effect of transition modeling. Figure 9 displays isocontours of $\alpha_v = 0.1$ near the tip of the wing. The more laminar the boundary layer becomes, the larger the cavity. Growth is predominantly observed in the positive lift ($y$) direction, i.e., in the direction of the suction side of the wing. This is in line with the observation by Maines and Arndt [45] that the vortex mainly interacts with the boundary layer on the suction side of the wing.

In order to quantify the cavity growth as function of inflow conditions, Fig. 10 presents the cavity radius over the cavity trajectory for all simulations. The cavity radius is not analyzed for $x/c_0 < 0.04$ because of the asymmetry of the vortex near the wing tip just above the boundary layer (see Fig. 9). With a decrease of turbulence quantities, the cavity length increases; the end point of the cavity of the LCTM simulation with $[I/\%, \nu_t/\nu] = 0.5$ lies 20% further downstream compared to the SST and LCTM simulation with $[I/\%, \nu_t/\nu] = 4.0$. The cavity radius at $x/c_0 \times 10 = 0.4$ is similar for all simulations, however the cavity's growth rate ($\partial\eta_c/\partial x$) increases with decreasing turbulent inflow conditions, likely because more high momentum (laminar) boundary layer fluid enters the vortex. The location of the maximum cavity radius is at $x/c_0 \times 10 \approx 1.0$ but moves slightly downstream with decreasing turbulence quantities. The LCTM simulation with $[I/\%, \nu_t/\nu] = 0.5$ results in a cavity which is about 20% thicker compared to the fully turbulent boundary layer. This is in line with the wetted flow results, and is a consequence of the assumption of the Schnerr–Sauer cavitation model which relates the mass transfer to the fluid static pressure. For $x/c_0 \times 10 > 1.0$, excessive turbulent diffusion resulting from the SST model causes the vortex to diffuse quickly. This results in a decreased size of the low pressure zone in the vortex core, and therefore a smaller cavity. The diffusion rate is similar for all simulations.

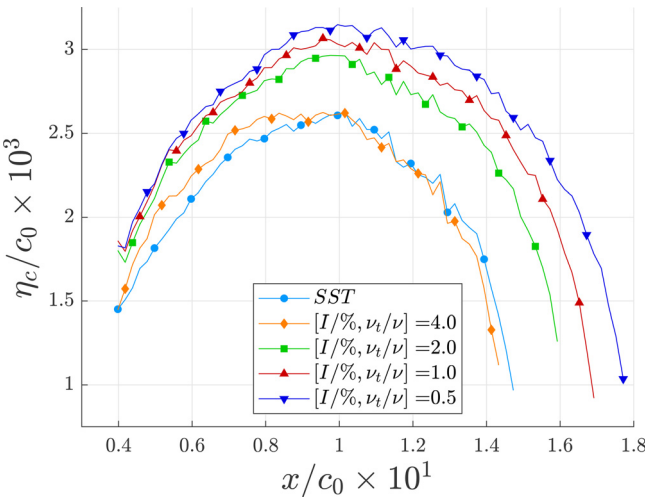


**Fig. 10 Cavity radius along the vortex trajectory for the SST and LCTM simulations for different turbulent inflow conditions. Cavity radius is defined using the isocontour of $\alpha_v = 0.1$.**

## 7 Effect of Turbulence Modeling

In this section, simulations using RANS closures were performed steady, while simulations using hybrid models were time-accurate. Based on the transient scanning technique, the results are temporally averaged over 3.3 nondimensional time units (defined as $t^* = t \times U_\infty/c_0$) after the statistically nonstationary period, this ensures that the statistical error is also at least one order of magnitude smaller than the discretization error. These start-up times for DDES and IDDES are 8.8 and 6.6 nondimensional time units, respectively, and are found to be independent of the timestep used [32]. Error bars in all graphs indicate the numerical uncertainties (spatial and temporal discretization, plus statistical). For the DDES and IDDES results, an estimate of the discretization uncertainties from a time-resolved SST simulation are used since error entanglement in hybrid models violates the assumptions made by the procedure to determine this uncertainty.

Simulations are performed at 9 deg so as to minimize the input uncertainty, since then transition occurs at the leading edge. All results shown are for the finest grid and timestep combination, i.e., $G_{1,9}$ and $\Delta t_1$. The vortex is analyzed at $x/c_0 = 0.5$ downstream of the tip. First, Secs. 7.1 and 7.2 consider wetted flow conditions. Thereafter, Sec. 7.3 concerns cavitating conditions.

**7.1 Wetted Vortex Prediction.** The lift coefficients obtained by all models, with the exception of EARSM, are within the validation uncertainty bounds compared to the experimental value, as shown in Table 2.

Figure 11 presents the azimuthal and axial velocity fields within the vortex for different turbulence models in sector I. The figure only includes the SST, RSM, and DDES results since results for KSKL and EARSM are comparable to SST, and IDDES is similar to DDES. Note that for all cases sector I is shown, with each result rotated by $\pi/2$ radians in the figure.

The azimuthal velocity fields for the RANS simulations are symmetric around the vortex axis of rotation. Furthermore, the magnitudes near the viscous core are substantially underpredicted, as already observed in Fig. 8. The RSM shows improved results compared to the other RANS models both in terms of magnitude and velocity distributions. However, the magnitudes around the viscous core are still underpredicted by about 15%. Asymmetry of the azimuthal velocity fields due to the roll-up process can be observed for the RSM and DDES simulations. Both in experiments and simulations, the magnitude is higher at side (b) of sector I compared to side (a) because the roll-up process is counterclockwise. The contour lines of the DDES simulation match the experimental measurements well, although the experimental results have a larger region of $u_\theta/U_\infty \approx 1.2$.

For all RANS simulations, deceleration of the flow in the vortex core models is observed, while the flow is accelerated in the experiments. The hybrid models also show deceleration near the

**Table 2 Value, numerical uncertainty, and modeling error of the lift coefficient for the different turbulence models at 9 deg AoA**

| | SST | KSKL | EARSM | RSM | DDES | IDDES | Exp. |
|---|---|---|---|---|---|---|---|
| $\overline{C}_L$ | 0.67 | 0.67 | 0.60 | 0.68 | 0.66 | 0.65 | 0.65 |
| $U_n(\overline{C}_L)/\%$ | 0.80 | 0.35 | 1.08 | 1.63 | 1.93 | 1.93 | 5.0 |
| $E_m(\overline{C}_L)/\%$ | 2.30 | 3.19 | −8.25 | 4.63 | 1.61 | −0.55 | |

Experiments by Pennings et al. [10].

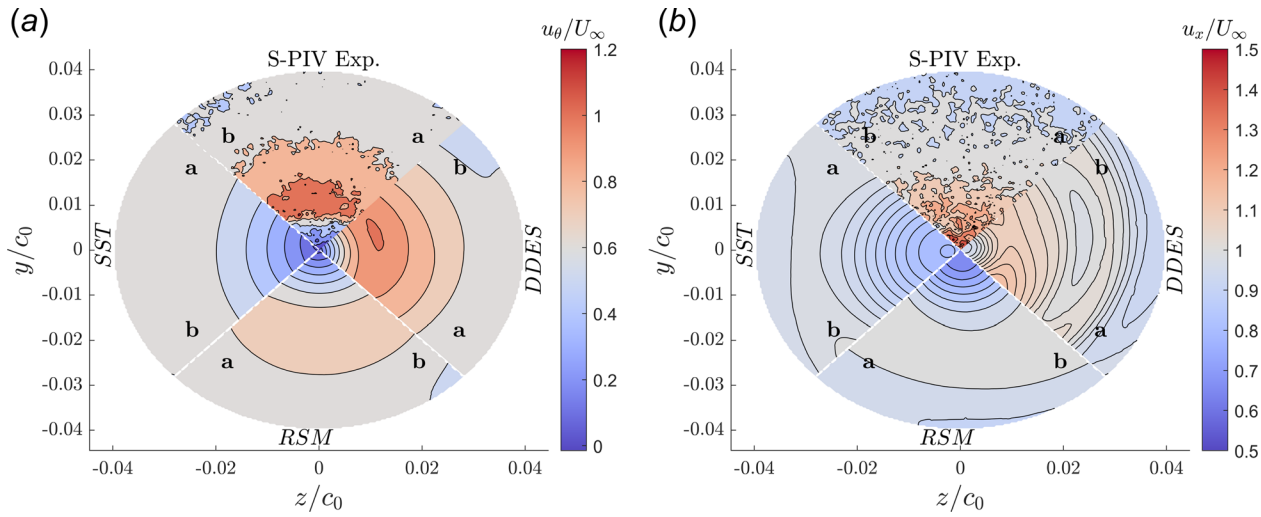


**Fig. 11 Azimuthaland axial velocity fields in sector I for SST, RSM, and DDES turbulence models at $x/c_0 = 0.5$ for wetted flow conditions. The S-PIV measurements are obtained by Ref. [10]. (*a*) $u_\theta/U_\infty$ and (*b*) $u_x/U_\infty$.**

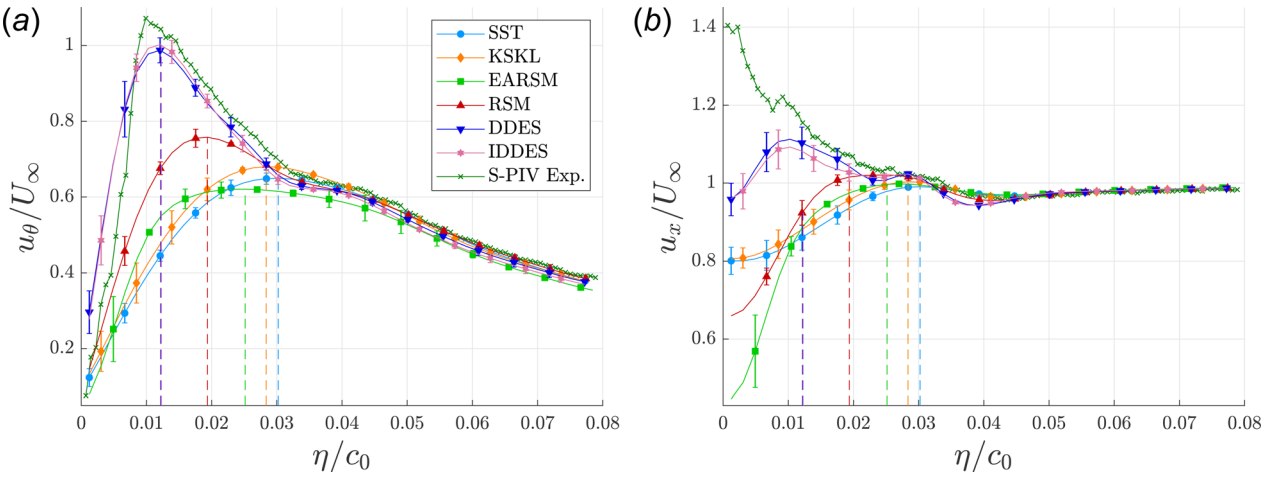


**Fig. 12 Azimuthaland axial velocity profiles in sector I for wetted flow conditions using SST, KSKL, EARSM, RSM, DDES, and IDDES turbulence models. Results sampled at $x/c_0 = 0.5$, vertical lines indicate the viscous core radius (location of maximum azimuthal velocity). The S-PIV measurements are obtained by Ref. [10]. (*a*) $u_\theta/U_\infty$ and (*b*) $u_x/U_\infty$.**

center of the vortex but match the axial velocity well just outside the core. The discrepancy at the vortex core can be related to the lower pressure gradient in streamwise direction compared to experiments, due to the use of slip-walls along the tunnel walls. Again, more asymmetry is present in the axial velocity fields predicted by RSM and DDES than for SST. Whether the asymmetry of the axial velocity field is also present in reality is difficult to conclude based on the available experimental measurement data.-The velocity distributions, circumferentially averaged around the vortex radius, are shown in Fig. 12 for the different turbulence models. The azimuthal and axial velocity profiles of the KSKL model match the experimental results better compared to the SST model. Still, the linear constitutive relation for the eddy viscosity yields excessive turbulent diffusion. It is observed that the EARSM does not improve results despite its nonlinear constitutive relationship. However, this comparison is biased since the wing circulation predicted by the EARSM is 10% lower compared to the other models (see Table 2). The lower circulation yields a weaker vortex and thus lower magnitudes of all velocities in the vortex. To compare them more accurately, one should compare the velocity profiles for a constant lift force instead. Nevertheless, it can be observed that the viscous core radius of the EARSM is smaller (and thus closer to the experiments) compared to SST and KSKL models. Also, the slope of the azimuthal velocity ($\partial u_\theta/\partial\eta$) for $\eta < \eta_v$ is better captured by EARSM than SST or KSKL. For the axial velocity, however, the flow is decelerated about 40% more compared to the SST and KSKL models, which cannot be explained by the underprediction of the lift. The same is observed for the RSM, which predicts the azimuthal velocity better compared to the SST and KSKL models. However, the axial velocity for $\eta/c_0 < 0.01$ is underpredicted 10% more relative to SST and KSKL. Furthermore, the viscous core radius is decreased compared to SST and KSKL, which is one of the reasons [17] obtained a good prediction of the pressure in a tip vortex. From the azimuthal velocity distributions, it is clear that the hybrid models predict a viscous core radius, which is closer to the experimental value compared to RANS. Both hybrid models accelerate almost all the axial flow in the vortex core (for $\eta/c_0 > 0.01$) as observed in the experiments. Although the discrepancy for $\eta/c_0 < 0.01$ is on average still 15%, it is an improvement over the other models, which decelerate the flow.

A validation exercise was made by utilizing the multivariate metric $r/r_{\text{ref}}$ at $x/c_0 = 0.50$, 0.74, and 1.14, the results of which are presented in Table 3. Only the local circumferentially averaged velocity fields are considered due to a uniform vector spacing in the S-PIV measurements. This causes the multivariate

**Table 3 Multivariate metric $r/r_{ref}$ of azimuthal and axial velocity profiles in sector I for different turbulence models**

| Velocity component | Location | SST | KSKL | EARSM | RSM | DDES | IDDES |
|---|---|---|---|---|---|---|---|
| Azimuthal | $x/c_0 = 0.50$ | 8.72 | 5.67 | 18.92 | 7.21 | 1.85 | 2.40 |
| | $x/c_0 = 0.74$ | 13.75 | 12.13 | 19.28 | 5.49 | 3.20 | 3.65 |
| | $x/c_0 = 1.14$ | 28.10 | 12.34 | 25.21 | 6.78 | 9.27 | 9.40 |
| Axial | $x/c_0 = 0.50$ | 3.83 | 4.38 | 7.54 | 3.13 | 1.71 | 1.87 |
| | $x/c_0 = 0.74$ | 4.16 | 5.23 | 19.28 | 8.03 | 2.02 | 1.96 |
| | $x/c_0 = 1.14$ | 6.20 | 9.58 | 19.66 | 6.55 | 4.35 | 4.50 |

metric to assign more "weight" to the freestream rather than to the region of interest (the vortex), since more points are located in the freestream. The multivariate metrics of the global flow fields would therefore result in distorted conclusions. The values reported in the table confirm observations previously made based on Fig. 12.

For the hybrid models, $r/r_{ref}$ is close to 1.0, but this increases for the locations further downstream due to numerical diffusion of $u_\theta$ and $u_x$. For the RANS models, $r/r_{ref} \gg 1.0$. The lowest values occur for the RSM. Note that from the velocity plots in Fig. 12, it seems that the azimuthal velocity is predicted better than the axial velocity, although the multivariant metric results imply the opposite. This is because Fig. 12 shows the absolute nondimensional velocity. The actual percentage error (on which the multivariant metric is based) is higher for the azimuthal velocity due to the lower magnitude, explaining the lower values of $r/r_{ref}$ for the axial velocity.

A further point of note is that the resolved Reynolds stresses in the hybrid simulations are found to be negligible compared to the unresolved stresses. In these simulations, the RANS statistical representation of turbulence, developed in the wing boundary layer, does not transfer to a resolved representation in the form of velocity fluctuations, due to commutation errors. The destruction of turbulence kinetic energy in the area where RANS and LES are blended should decrease the stability of the flow whereby velocity fluctuations in the LES region could develop. It is observed that the absence of unsteady effects in the flow field near the wing or in the freestream prevent this development [46]. For both methods, the viscous core lies completely inside the LES region; for DDES, the LES region corresponds to $\eta/c_0 \lesssim 0.05$, while for IDDES $\eta/c_0 \lesssim 0.2$. The absence of velocity fluctuations implies that the results still contain a modeling error, despite matching the experiments reasonably well. This behavior is in contrast to the results by Paskin, who did observe velocity fluctuations, yet the inflow conditions used in that work are unknown [13].

**7.2 The Role of Modeled Turbulent Diffusion.** As introduced in Sec. 1, previous researchers encountered excessive turbulent diffusion of the vortex when simulating the cavitating tip vortex generated by the wing, leading to an underpredicted cavity length. This is mainly related to overprediction of eddy viscosity, since this amplifies the diffusion term in the momentum equations.

Figure 13 shows a different behavior for the eddy viscosity profiles along the vortex radius for the different turbulence models in wetted flow conditions. The eddy viscosity for the SST and KSKL models increases toward the vortex core, and is more than one order of magnitude higher compared to the hybrid models. In $k-\omega$ based models, the eddy viscosity is proportional to $k/\omega$, while for the KSKL model the eddy viscosity is proportional to $kL/\sqrt{k}$ (Eq. (12)). The turbulence kinetic energy for the RANS models is found to be more than a factor of five higher compared to the hybrid models. Furthermore, the specific dissipation rate is inversely proportional to $k$. Together, this leads to a high eddy viscosity and more turbulent diffusion near the vortex center. The peak in eddy viscosity is within the viscous core radius, while for the EARSM it is clearly outside the viscous core. For EARSM,

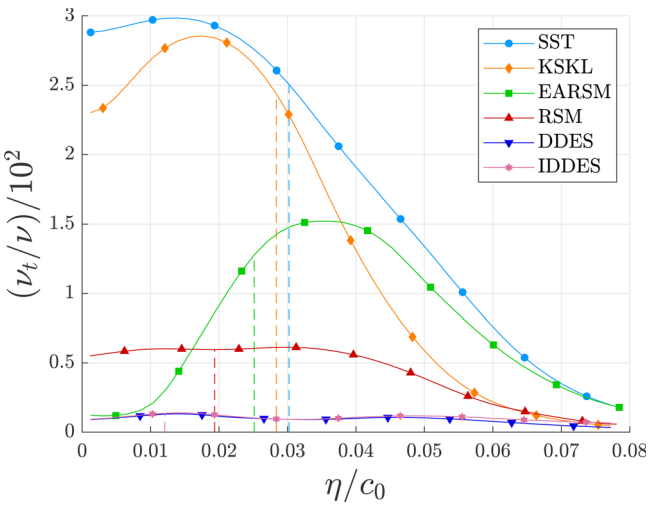


**Fig. 13 Radial distribution of eddy viscosity ratio in sector I for wetted flow conditions using SST, KSKL, EARSM, RSM, DDES, and IDDES turbulence models. Results sampled at $x/c_0 = 0.5$, vertical lines indicate the viscous core radius (location of maximum azimuthal velocity).**

the values are comparable to SST for $\eta/c_0 \geq 0.04$, but decrease to the values for the hybrid models toward the vortex center. This decrease near the center is related to an increase in the specific dissipation rate, and the dependence on $C_\mu$ which varies in space as $C_\mu \propto I_\omega \propto \Omega^*_{ij} \propto \tau \propto 1/\omega$ (see Eq. (17)). Through this relation, $\nu_t \propto 1/\omega^2$, leading to an amplification of the effect of the increased specific dissipation. The eddy viscosity predicted by the RSM lies between the values for the SST, KSKL and hybrid models, but remains constant for $\eta/c_0 \leq 0.04$. The eddy viscosity predicted by the hybrid models remains low across the vortex radius due to the increased destruction of turbulence kinetic energy (a consequence of a decrease in the DES length scales, see Eqs. (26) and (27)).

In previous work, the axial velocity deficit (deceleration) in the vortex is also explained by the high eddy viscosity [11,12], yet the current results contradict that explanation. In the region $\eta/c_0 < 0.01$, $\nu_t$ from the EARSM is comparable in magnitude to the hybrid models. The axial velocity predicted by EARSM, however, is more than 50% lower (see Fig. 12). In the case of the EARSM, the axial velocity deficit is instead related to the nonlinear term, $a_{ij}$, in the definition of the Reynolds stress tensor (Eq. (6)). This term redistributes the turbulence kinetic energy over the different normal components of the tensor. This can be observed in Fig. 14, where the unresolved (modeled) Reynolds normal stresses for the EARSM simulation are dominant in the $x$ and $y$ directions. Their distributions vary strongly along the radius. The $x$ component is highest just near the center of the vortex, which explains the large diffusion of axial velocity. The same holds for the RSM, although the differences are then smaller. For the SST, KSKL, DDES, and IDDES models, $u_i'u_i'$ has the same magnitude in each direction conforming their expected isotropic nature. The differences in the modeled Reynolds stresses are

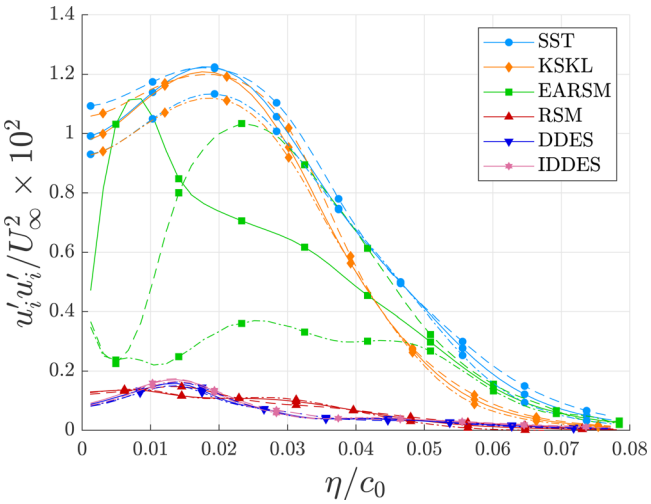


**Fig. 14 Modeled normal Reynolds stress profiles in sector I for wetted flow conditions SST, KSKL, EARSM, RSM, DDES, and IDDES turbulence models. Solid lines indicate $u'u'$, dashed lines $v'v'$, and dashed-dotted lines $w'w'$. Results sampled at $x/c_0 = 0.5$.**

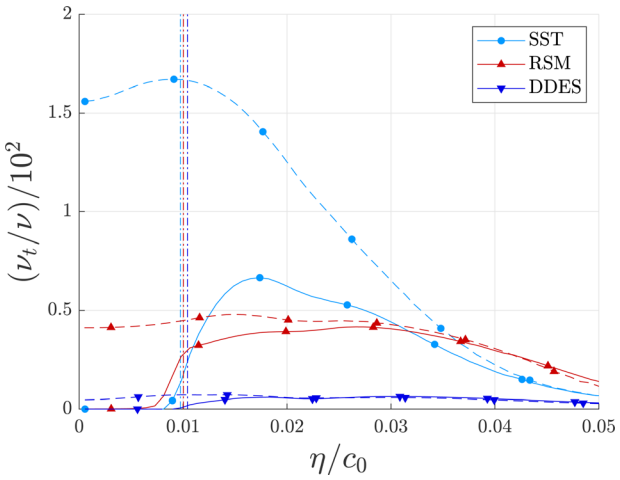


**Fig. 15 Radial distribution of eddy viscosity ratio in sector I for SST, RSM, and DDES turbulence models in cavitating (solid lines) and wetted flow (dashed lines) conditions at $x/c_0 = 0.25$. Vertical lines indicate the cavity radius ($\alpha_v = 0.1$).**

proportional to the differences in eddy viscosity, as expected based on Eq. (6).

**7.3 Turbulence Model Behavior in Cavitating Flow.** In literature, often isocontours of the vapor pressure are used to indicate the region where cavitation can be expected from a wetted flow simulation (see, e.g., Refs. [11] and [12]). However, the effect of cavitation on other flow variables, and therefore implicitly on the cavity size, has received less attention. In order to investigate this, the different turbulence models were also applied for cavitating flow simulations and compared to the results of Sec. 7.1. In this work, we focus on the interaction of the turbulence and cavitation models. All results presented were obtained for the finest grid and timestep, using the same numerical settings as in Sec. 7.1. The results are compared at $x/c_0 = 0.25$. No validation was possible since the closest plane [10] measured in cavitating conditions with respect to the tip is $x/c_0 = 1.14$, and the cavities predicted by all models are already diffused upstream of this point.

Table 4 shows that the cavity length in cavitating conditions is significantly longer compared to the "cavity" length in wetted flow conditions, for all models investigated. This is related to the effect of the cavity on the eddy viscosity, as shown in wetted and cavitating conditions in Fig. 15. Note that the eddy viscosity is normalized by the viscosity of the pure liquid rather than the mixture. The results for the KSKL, EARSM, and IDDES simulations are excluded since they are similar to the SST, RSM, and DDES simulations, respectively. The eddy viscosity becomes almost zero inside the cavity and is reduced by a factor of two just outside the cavity, due to a decrease in $k$ and an increase in $\omega$.

**Table 4 Quantitative comparison of cavity length in wetted and cavitating flow conditions using different turbulence models**

| Turbulence model | $x_{\text{end,wet}}/c_0$ | $x_{\text{end,cav}}/c_0$ | $x_{\text{end,cav}}/x_{\text{end,wet}}$ |
|---|---|---|---|
| SST | 0.288 | 0.461 | 1.595 |
| KSKL | 0.321 | 0.481 | 1.498 |
| EARSM | 0.303 | 0.510 | 1.687 |
| RSM | 0.505 | 0.859 | 1.702 |
| DDES | 0.980 | 1.104 | 1.126 |
| IDDES | 0.961 | 1.098 | 1.142 |

To understand what happens when fluid enters the cavity, the production ($P_k$) and destruction ($D_k$) terms of the $k$ equation for the SST, RSM and DDES models are considered (see Sec. 3.1 for their definitions). Figure 16 shows that $P_k$ decreases toward zero within the cavity and is reduced outside the cavity compared to wetted flow conditions. $D_k$ is less affected inside the cavity, resulting in a strong reduction of modeled turbulence in and around the cavity. This imbalance between $P_k$ and $D_k$ originates from the lack of velocity gradients (and thus strain rate) in and around the cavity. Since $P_k$ is directly related to the magnitude of the strain rate tensor, it can decrease rapidly, while $D_k$ is only dependent on the two turbulence quantities meaning an abrupt drop is not expected. The lack of velocity gradients is due to a constant pressure within the cavity as can be seen in Fig. 17. The pressure coefficient levels out to a value just below the cavitation number, as the cavitation model keeps increasing the vapor volume fraction. The absence of velocity gradients yields constant axial and azimuthal velocities in the cavity (the magnitude of the axial component of the vorticity vector is also almost zero meaning the flow is also irrotational), almost no eddy viscosity since the $P_k$ vanishes while $D_k$ remains, and much lower Reynolds normal stresses in the cavity, due to Eq. (6). This results in the vapor flow in the cavity having the same characteristics as a potential flow. No pressure (nor velocity) measurements of the flow within a tip vortex cavity were found in the literature to verify or disprove this finding.

## 8 Conclusions

The elliptical Arndt wing is a well-known test case for studying cavitating tip vortices. In literature, the underprediction of the tip vortex size is commonly attributed to numerical diffusion and an overprediction of eddy viscosity. In this study, it was shown, both theoretically and numerically, that the assumption of a fully turbulent boundary layer in CFD simulations also contributes to the underprediction of the tip vortex cavity size, especially for cases where the inflow turbulence quantities strongly affect the location of transition. The iterative, statistical, spatial, and temporal discretization errors were estimated and found to be below 2% for the lift coefficient. The results are compared against measurements by Pennings et al. [10].

The use of a transition model, while controlling the boundary layer thickness using different turbulent inflow conditions, predicts a decrease of the viscous core radius, and consequently the pressure in the vortex, of 20% for the wing at 5 deg AoA in wetted flow conditions. At 9 deg AoA, deg reduces to 7%, due to transition occurring at the leading edge of the wing. Similar behavior

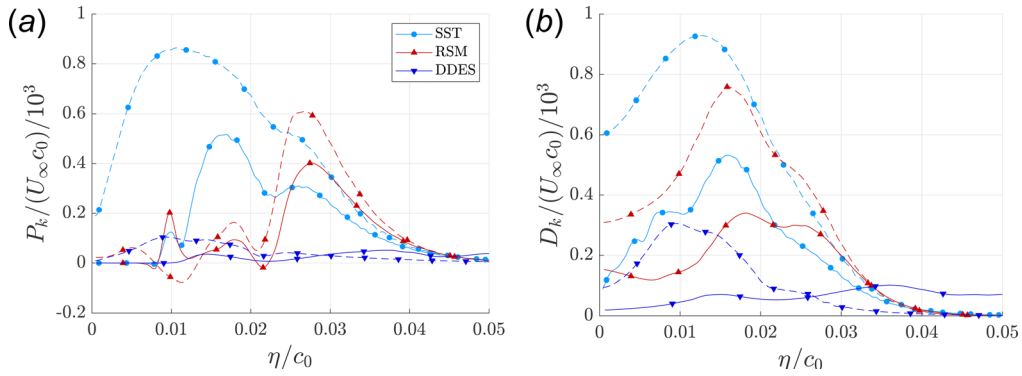


**Fig. 16 Radial distributions of production, $P_k$, and destruction, $D_k$, terms of $k$ transport equation for SST, RSM, and DDES turbulence models for cavitating (solid lines) and wetted (dashed lines) flow, sampled at $x/c_0 = 0.25$ in sector I. (*a*) $P_k$ and (*b*) $D_k$.**

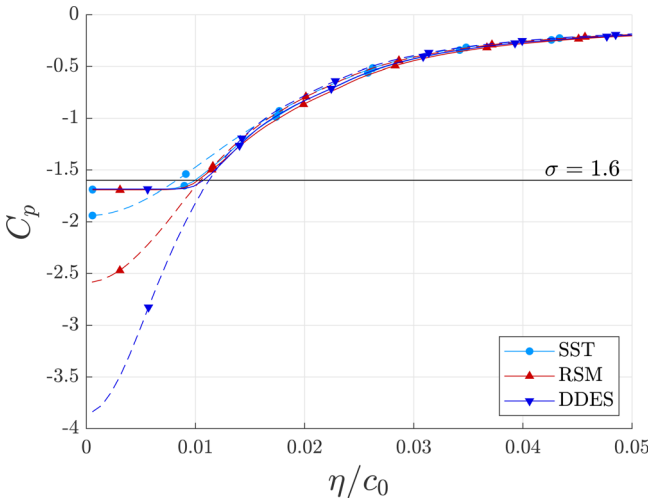


**Fig. 17 Radial distribution of pressure coefficients in sector I at $x/c_0 = 0.25$ for SST, RSM, and DDES turbulence models in cavitating (solid lines) and wetted (dashed lines) flow conditions**

was found for the increase in vapor volume in cavitating flow conditions. Considering the known shortcomings of the SST model in predicting vortical flows, it is expected that further improvements to the results could be obtained by applying the LCTM model in combination with other turbulence models.

To compare different turbulence models, an AoA of 9 deg was udeg due to the transition occurring at the leading edge, regardless of the inflow condition. The lift coefficients predicted by the SST, KSKL, RSM, DDES, and IDDES turbulence models were within the uncertainty bounds of the experimental results. The EARSM simulation underpredicted the lift, which biases the comparison of velocity profiles in the vortex. Furthermore, the anisotropy in the normal Reynolds stresses in the EARSM simulation yielded a large axial velocity deficit. Although the velocity profiles in the vortex predicted by DDES and IDDES are close to the experimental results, the outcome still suffers from commutation errors. Specifying time-varying stochastic velocity fluctuations in the inflow could stimulate the development of turbulent structures in the LES regions. This could allow the effect of turbulent velocity fluctuations on the cavity to be assessed.

It is shown that the presence of cavitation reduces turbulent diffusion in the vortex due to a constant pressure inside the vapor region. The absence of velocity gradients in all directions yields constant axial and azimuthal velocities in the cavity, almost zero eddy viscosity, and lower Reynolds normal stresses. Whether this is physically plausible is uncertain, yet no evidence to verify or disprove this was found in literature.

## Acknowledgment

This research was financially supported by the Netherlands Organisation for Scientific Research, NWO, as part of the NOISOURCE project (ALWTW.2016.008), and by the Dutch Ministry of Economic Affairs. We thank Rui Lopes for sharing his knowledge regarding transition modeling, and Johan Bosschers for his comments on the results. Part of this work was conducted as a M.Sc. thesis at the Faculty of Aerospace Engineering at Delft University of Technology.

## Funding Data


- NOW (Funder ID: 10.13039/501100003246).
- Dutch Ministry of Economic Affairs (Funder ID: 10.13039/501100003195).


## References


[1] Hildebrand, J. A., 2009, "Anthropogenic and Natural Sources of Ambient Noise in the Ocean," Mar. Ecol.: Prog. Ser., **395**, pp. 5–20.
[2] Frisk, G. V., 2012, "Noiseonomics: The Relationship Between Ambient Noise Levels in the Sea and Global Economic Trends," Sci. Rep., **2**(1), pp. 437–441.
[3] DNV GL, 2015, "Living and Working Conditions, Section 1 Comfort Class," Rules for Classification, Ships, DNV GL, Høvik, Norway, Chap. 8.
[4] De Lorenzo, F., and Biot, M., 2006, "Noise and Vibration: Comfort Standards Evolving in the Wrong Direction?," Nav. Archit., pp. 36–39.
[5] van Wijngaarden, E., Bosschers, J., and Kuiper, G., 2005, "Aspects of the Cavitating Propeller Tip Vortex as a Source of Inboard Noise and Vibration," ASME Paper No. FEDSM2005-77271.
[6] Bosschers, J., 2018, "Propeller Tip-Vortex Cavitation and Its Broadband Noise," Ph.D. thesis, University of Twente, Enschede, The Netherlands.
[7] Carlton, J., 2018, *Marine Propellers and Propulsion*, Elsevier Butterworth-Heinemann, Oxford, UK.
[8] Higuchi, H., Arndt, R., and Rogers, M., 1989, "Characteristics of Tip Vortex Cavitation Noise," ASME J. Fluids Eng., **111**(4), pp. 495–501.
[9] Dacles-Mariani, J., Zilliac, G. G., Chow, J. S., and Bradshaw, P., 1995, "Numerical/Experimental Study of a Wingtip Vortex in the Near Field," AIAA J., **33**(9), pp. 1561–1568.
[10] Pennings, P., Westerweel, J., and Van Terwisga, T., 2015, "Flow Field Measurement Around Vortex Cavitation," Exp. Fluids, **56**(11), pp. 206–219.
[11] Schot, J. J., Pennings, P. C., Pourquie, M., and Van Terwisga, T. J., 2014, "Modelling of Tip Vortex Cavitation for Engineering Applications in OpenFOAM," Proceedings-WCCM XI: 11th World Congress on Computational Mechanics (CIMNE), Barcelona, Spain, July 20–25, pp. 1–12.
[12] Asnaghi, A., 2018, "Computational Modelling for Cavitation and Tip Vortex Flows," Ph.D. thesis, Chalmers University of Technology, Gothenburg, Sweden.
[13] Paskin, L., 2018, "A Numerical Assessment of Turbulence Modeling in Tip Vortex Flows at Cavitating Conditions," Master's thesis, Ecole Centrale de Nantes, Nantes, France.
[14] Arndt, R., Arakeri, V., and Higuchi, H., 1991, "Some Observations of Tip-Vortex Cavitation," J. Fluid Mech., **229**(1), pp. 269–289.
[15] Pennings, P., Bosschers, J., Westerweel, J., and Van Terwisga, T., 2015, "Dynamics of Isolated Vortex Cavitation," J. Fluid Mech., **778**, pp. 288–313.

[16] Asnaghi, A., Bensow, R., and Svennberg, U., 2017, "Comparative Analysis of Tip Vortex Flow Using RANS and LES," Seventh International Conference on Computational Methods in Marine Engineering, Nantes, France, June 15–17, pp. 1–12.
[17] Pereira, F. S., Eça, L., and Vaz, G., 2019, "Simulation of Wingtip Vortex Flows With Reynolds-Averaged Navier–Stokes and Scale-Resolving Simulation Methods," AIAA J., **57**(3), pp. 932–948.
[18] Menter, F. R., Kuntz, M., and Langtry, R., 2003, "Ten Years of Industrial Experience With the SST Turbulence Model," Turbul., Heat Mass Transfer, **4**(1), pp. 625–632.
[19] Menter, F. R., Egorov, Y., and Rusch, D., 2006, "Steady and Unsteady Flow Modelling Using the k-$\sqrt{k}$L Model," *ICHMT Digital Library Online*, Begell House, Danburry, CT.
[20] Wallin, S., and Johansson, A. V., 2000, "An Explicit Algebraic Reynolds Stress Model for Incompressible and Compressible Turbulent Flows," J. Fluid Mech., **403**, pp. 89–132.
[21] Eisfeld, B., and Brodersen, O., 2005, "Advanced Turbulence Modelling and Stress Analysis for the DLR-F6 Configuration," AIAA Paper No. 2005-4727.
[22] Spalart, P. R., Deck, S., Shur, M. L., Squires, K. D., Strelets, M. K., and Travin, A., 2006, "A New Version of Detached-Eddy Simulation, Resistant to Ambiguous Grid Densities," Theor. Comput. Fluid Dyn., **20**(3), pp. 181–196.
[23] Shur, M. L., Spalart, P. R., Strelets, M. K., and Travin, A. K., 2008, "A Hybrid RANS-LES Approach With Delayed-DES and Wall-Modelled LES Capabilities," Int. J. Heat Fluid Flow, **29**(6), pp. 1638–1649.
[24] Maines, B. H., and Arndt, R., 1997, "Tip Vortex Formation and Cavitation," ASME J. Fluids Eng., **119**(2), pp. 413–419.
[25] McCormick, B., 1962, "On Cavitation Produced by a Vortex Trailing From a Lifting Surface," ASME J. Basic Eng., **84**(3), pp. 369–378.
[26] Lamb, H., 1932, *Hydrodynamics*, 6th ed., Cambridge University Press, Cambridge, UK.
[27] Kaden, H., 1931, "Aufwicklung Einer Unstabilen Unstetigkeitsfläche," Arch. Appl. Mech., **2**(2), pp. 140–168.
[28] Moore, D., 1974, "A Numerical Study of the Roll-Up of a Finite Vortex Sheet," J. Fluid Mech., **63**(2), pp. 225–235.
[29] Hellsten, A. K., 2005, "New Advanced $k-\omega$ Turbulence Model for High-Lift Aerodynamics," AIAA J., **43**(9), pp. 1857–1869.
[30] Gritskevich, M. S., Garbaruk, A. V., Schütze, J., and Menter, F. R., 2012, "Development of DDES and IDDES Formulations for the k-$\omega$ Shear Stress Transport Model," Flow, Turbul. Combust., **88**(3), pp. 431–449.
[31] Langtry, R. B., and Menter, F. R., 2009, "Correlation-Based Transition Modeling for Unstructured Parallelized Computational Fluid Dynamics Codes," AIAA J., **47**(12), pp. 2894–2906.
[32] Hirt, C. W., and Nichols, B. D., 1981, "Volume of Fluid (VoF) Method for the Dynamics of Free Boundaries," J. Comput. Phys., **39**(1), pp. 201–225.
[33] Schnerr, G. H., and Sauer, J., 2001, "Physical and Numerical Modeling of Unsteady Cavitation Dynamics," Fourth International Conference on Multiphase Flow (ICMF), Vol. 1, New Orleans, LA, May 27–June 1, pp. 1–12.
[34] Liebrand, R., 2019, "Tip Vortex Modelling for Cavitation Noise Applications: A Verification and Validation Study in ReFRESCO," Master's thesis, Delft University of Technology, Delft, The Netherlands.
[35] Eça, L., and Hoekstra, M., 2014, "A Procedure for the Estimation of the Numerical Uncertainty of CFD Calculations Based on Grid Refinement Studies," J. Comput. Phys., **262**, pp. 104–130.
[36] Brouwer, J., Tukker, J., and Van Rijsbergen, M., 2015, "Uncertainty Analysis and Stationarity Test of Finite Length Time Series Signals," Fourth International Conference on Advanced Model Measurement Technology for the Maritime Industry (AMT 15), Istanbul, Turkey, Oct. 7–9, pp. 1–14.
[37] Arndt, R. E., and Keller, A. P., 1992, "Water Quality Effects on Cavitation Inception in a Trailing Vortex," ASME J. Fluids Eng., **114**(3), pp. 430–438.
[38] ASME, 2009, *Standard for Verification and Validation in Computational Fluid Dynamics and Heat Transfer*, ASME, New York.
[39] Hills, R. G., 2006, "Model Validation: Model Parameter and Measurement Uncertainty," ASME J. Heat Transfer, **128**(4), pp. 339–351.
[40] Higuchi, H., Quadrelli, J. C., and Farell, C., 1987, "Vortex Roll-Up From an Elliptic Wing at Moderately Low Reynolds Numbers," AIAA J., **25**(12), pp. 1537–1542.
[41] Vaz, G., Jaouen, F., and Hoekstra, M., 2009, "Free Surface Viscous Flow Computations: Validation of URANS Code FRESCO," ASME Paper No. OMAE2009-79398.
[42] Liebrand, R., Klapwijk, M., Lloyd, T., Vaz, G., and Lopes, R., 2019, "A Sensitivity Analysis of CFD Transition Modelling in the Context of Vortex Roll-Up Prediction," Proceedings of Eighth International Conference on Computational Methods in Marine Engineering, Gothenburg, Sweden, May 13–15, pp. 1–12.
[43] Lloyd, T., Vaz, G., Rijpkema, D., and Reverberi, A., 2017, "Computational Fluid Dynamics Prediction of Marine Propeller Cavitation Including Solution Verification," Fifth International Symposium on Marine Propulsors, Espoo, Finland, June 12–15, pp. 1–13.
[44] Asnaghi, A., Bensow, R. E., and Svennberg, U., 2017, "Implicit Large Eddy Simulation of Tip Vortex on an Elliptical Foil," Fifth International Symposium on Marine Propulsion (SMP), Espoo, Finland, June 12–15, pp. 1–8.
[45] Maines, B., and Arndt, R. E., 1997, "The Case of the Singing Vortex," ASME J. Fluids Eng., **119**(2), pp. 271–276.
[46] Klapwijk, M., Lloyd, T., Vaz, G., and van Terwisga, T., 2020, "Evaluation of Scale-Resolving Simulations for a Turbulent Channel Flow," Comput. Fluids, **209**, p. 104636.